Chapter 5

Second-order Effects

There are more interesting research topics and techniques than what is well known in application of intracavity second-order effects. Harmonic generation and phase matching had been applied on frequency conversion in many fields for industry and research. In addition to frequency-doubled high-peak-power pulse laser, noncollinear second harmonic generation of laser in random domain structures can be used to explore the spatial structure of two-dimensional disordered wave functions with weak localization. The statistics of the experimental near-field patterns agree very well with the theoretical distributions. This result and other studies in the experiment also confirms the possibility of using conical SHG as a diagnostic tool for topographical characterization of crystals. There is one other topic that is important in seconder-order nonlinear effect, optical parametric amplifier and oscillator. Through the techniques of optical parametric oscillator pumped by a passively Q-switched Nd:YAG laser in a shared cavity configuration, we present a compact efficient eye-safe laser for modern military requirement. A signal pulse of 3.3 mJ energy at 1573-nm wavelength with a peak power of 150 kW was achieved. The effective conversion efficiency with respective to the optimized 1064-nm Q-switched pulse energy was as high as 51%.

5.1 Second-order Effects and Frequency Conversion [B6,B2]

Effects related to second-order nonlinear interaction are second harmonic generation (SHG), sum and difference frequency (frequency mixing), optical rectification, phase matching (PM),optical parametric amplifires and oscillators (OPA and OPO), Pockels' effect, and electro-optical beam deflection etc. The equation which formulate the nonlinear polarization of medium is $\boldsymbol{P}(\boldsymbol{r},t) = \varepsilon_0 \chi^{(1)}\boldsymbol{E}(\boldsymbol{r},t) + \varepsilon_0 \chi^{(2)}\boldsymbol{E}^2(\boldsymbol{r},t) + \varepsilon_0 \chi^{(3)}\boldsymbol{E}^3(\boldsymbol{r},t) + \ldots = \boldsymbol{P}_{linear}(\boldsymbol{r},t) + \boldsymbol{P}_{nonlinear}(\boldsymbol{r},t)$, where E is the electric

field of the light. Second-order nonlinear susceptibility $\chi^{(2)}$ and PM including Birefrigent Phase Matching and Quasi-Phase Matching are basis of second-order frequency conversion. The theories about nonlinear frequency conversion were refined well and simply in [43].

5.2 Noncollinear SHG, Random Scattering, Pattern Formation, and Weak Localization

5.2.1 Introduction to Pattern Formation and Random Laser

To find patterns on animal's body, shell, or plant's arrangement is easy to nose out something interesting. Gorgeous fractal or kaleidoscopic patterns can be produced by simple mathematic equations or found out in living physics phenomena. Complex dynamics systems can also have their won specific patterns. Pattern formation is a spontaneous outpouring of spatial order, which may imply a lot of information behind patterns [44].

Light amplification achieved by the random scattering of light in a laser material without cavity mirrors is the typical Random laser. As photons scatters through the structure, they excite other atoms and stimulate them to emit coherent photons. The material itself plays the role of the reflecting mirrors in the distributed cavity [45].

5.2.2 Introduction to Weak Localization and Long-range Correlation in Disordered Wave Functions from Conical SHG

Interference effects between scattered waves lead to striking phenomena beyond the radiative transfer treatment and diffusion theory [1]. Weak localization is a hallmark of interference of multiply scattered waves in disordered media [2-4] and is a direct consequence of the constructive interference between reciprocal paths in wave scattering [5]. The phenomenon of weak localization has been extensively studied in coherent backscattering from colloidal suspension [6], strongly scattering powders [7], cold atom gases [8], two-dimensional (2D) random systems [9], randomized laser materials [10], disordered liquid crystals [11], and disordered microcavities [12]. Especially, microwave experiments have provided direct observation of quantum wave functions in disordered quantum billiards [13]. Even so, there have been few experimental studies of quantum disordered wave functions because of their lack of accessibility.

The underlying wave nature of the particles leads to the striking features that the

propagation of electrons in conducting devices shows many similarities with random multiple scattering of light in disordered media [2-4]. This relevance stimulated active research in the propagation of light waves in random scattering media since the 1980s [6]. Recently, it has been observed that multiple scattering of laser light in a microdomained nonlinear crystal constitutes a novel mechanism for conical second harmonic generation (SHG) [14]. The coherent wave in laser cavities enables one to achieve very precise measurements of intensity patterns. Nevertheless, experiments on the spatial structure of disordered wave functions with conical SHG have never been realized as yet.

In next section, we originally develop an intracavity conical SHG scheme to explore the spatial structure of 2D disordered wave functions with weak localization. By using a nonlinear crystal with extended defects, the conical SHG is efficiently produced from a Q-switched laser with intracavity frequency doubling. The near-field patterns of the conical SHG beams evidently represent the wave functions of disordered quantum systems. The statistics of the wave functions are found to be in quantitative agreement with the supersymmetry sigma model [15]. More importantly, the analysis of the intensity correlation for the experimental patterns reveals that the localization effects significantly enhance the magnitude of the long-range correlation.

5.2.3 Manifestation of Weak Localization and Long-range Correlation in Disordered Wave Functions from Conical SHG

In the past few years, a new nonlinear crystal family of calcium oxyborates such as $GdCa_4O(BO_3)_3$ (GdCOB) and $YCa_4O(BO_3)_3$ (YCOB), has been developed for efficient SHG and other parametric processes in various fields [16]. The optical properties of the nonlinear crystals are greatly affected by their structural imperfection that is strongly dependent on the material preparation and the growth conditions. Recent investigations [17] revealed that the disordered domain structures may be spontaneously present in nominal GdCOB samples which do not contain any macroscopic defects and cracks. Intriguingly, the presence of an appropriate distribution of disordered domains allows broadband frequency conversion processes without any temperature or angular tuning of the crystal, especially for conical SHG. Here we used a GdCOB crystal with moderate random defect domains to investigate the spatial structure of disordered wave functions. Figure 5.1 depicts the experimental configuration for the diode-pumped actively Q-switched Nd:YAG laser with intracavity SHG in the GdCOB crystal. The input mirror is a 500-mm

radius-of-curvature concave mirror with antireflection coating at 808 nm on the entrance face (R<0.2%), high-reflection coating at 1064 nm (R>99.8%) and 532 nm (R>99%) and high-transmission coating at 808 nm on the other surface (T>90%). The output coupler is a flat mirror with high-reflection coating at 1064 nm (R>99.8%) and high-transmission coating at 532 nm (T>85%). The pump source was an 808-nm fiber-coupled laser diode with a core diameter of 800 μm, a numerical aperture of 0.16 and a maximum output power of 10 W. Focusing lens with 12.5-mm focal length and 90% coupling efficiency was used to re-image the pump beam into the laser crystal. The laser medium was a 0.8-at.% Nd^{3+}:YAG crystal with a length of 10 mm. The GdCOB crystal was cut for type-I frequency doubling on the Z axis ($\theta=0^o$, $\phi=0^o$) with a length of 2 mm and a cross section of 3 mm × 3 mm. Both sides of the Nd:YAG and GdCOB crystals were coated for antireflection at 1064 nm (R<0.2%). The diameters of the laser beams were approximately 580 μm and 500 μm in the Nd:YAG and GdCOB crystals, respectively. The 30-mm-long acousto-optic Q-switch (NEOS Technologies) had antireflection coatings at 1064-nm on both faces and was driven at a 27.12 MHz center frequency with 15.0-W of RF power. The laser cavity length was approximately 10 cm.

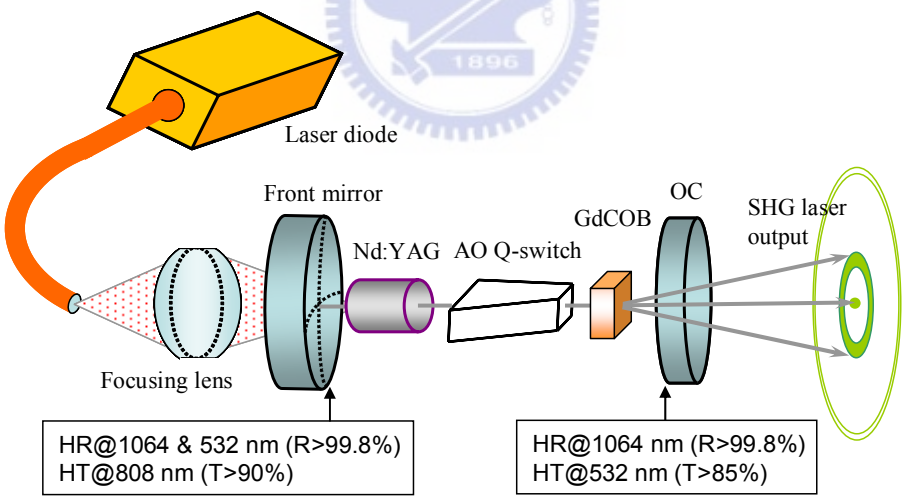

Fig. 5.1. The experimental configuration for the diode-pumped actively Q-switched Nd:YAG laser with intracavity second harmonic generation (SHG) in the GdCOB crystal.

The pulse repetition rate for the Q-switched pulses was fixed at 20 kHz. The lasing thresholds for the axial and conical SHG beams were nearly the same and

approximately 3W. The typical far-filed pattern was shown in Fig. 5.2(a). At a pump power of 8 W, the output powers of both the axial and conical SHG beams were on the order of 1 mW. The phase-matching condition for the conical SHG in a nonlinear crystal with disordered domain structures is generally written as $\vec{k}_1 + \vec{k}_1' = \vec{k}_2$, as shown in Fig. 5.2(b), where $\vec{k}_1$ is the axial fundamental beam, $\vec{k}_1'$ is the scattered off-axis fundamental beam, and $\vec{k}_2$ is the phase-matched off-axis SHG beam. The cone angle φ is determined by the effective refractive indices. Experimental results revealed that the cone angles of the far-field patterns were almost the same for all the transverse positions of the GdCOB crystal. Even so, the near-field patterns were found to be profoundly related to the topographical characterization of the nonlinear crystal.

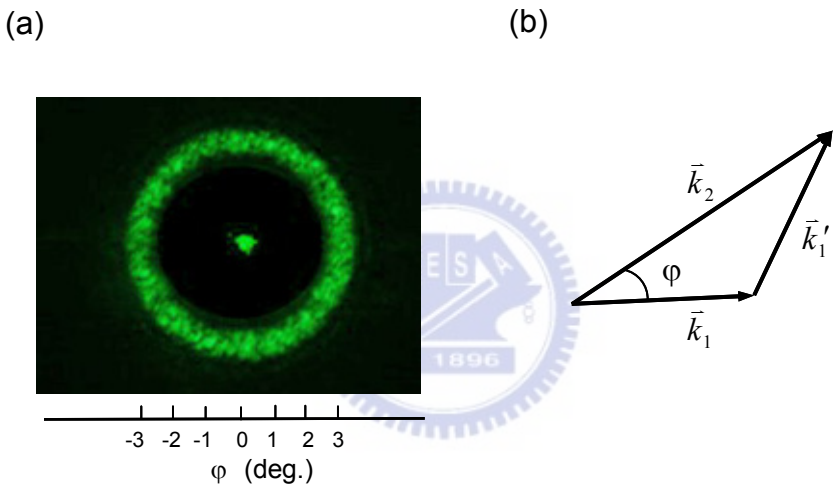

Fig. 5.2. (a) The typical far-field pattern of conical SHG. (b) Phase-matching diagram for conical SHG process in which $\vec{k}_1$ is the axial fundamental beam, $\vec{k}_1'$ is the scattered off-axis fundamental beam, and $\vec{k}_2$ is the phase-matched off-axis SHG beam.

Figures 5.3(a)-(d) show four examples of the near-field wave patterns measured at different transverse positions of the GdCOB crystal. It can be seen that the experimental near-field patterns $|\Psi(\vec{r})|^2$ exhibits a network of quasi-linear ridge structures which result from the superposition of monochromatic plane waves with random directions and phases in two dimensions, as discovered by O'Connor, Gehlen, and Heller [18]. Note that the paraxial propagation and the phase-matching

condition lead to the present conical SHG to be a kind of 2D random scattering process. The quasi-linear ridge patterns should be distinguished from the ordinary speckle patterns that are a 2D projection of the light formed by the superposition of monochromatic plane waves with random directions and phases in three dimensions. In other words, the ordinary speckle pattern has a spread in the magnitudes of the projected wave vectors, whereas the quasi-linear ridge pattern consists of only a nearly constant transverse wave vector. With the cone angle of the far-field patterns, the present near-field patterns are associated with a superposition of random plane waves with the transverse wave number $K = k_2 \sin\varphi$. To our knowledge, this is the first time that the near-field patterns of conical SHG are used to visualize the spatial structures of the quantum disordered wave functions.

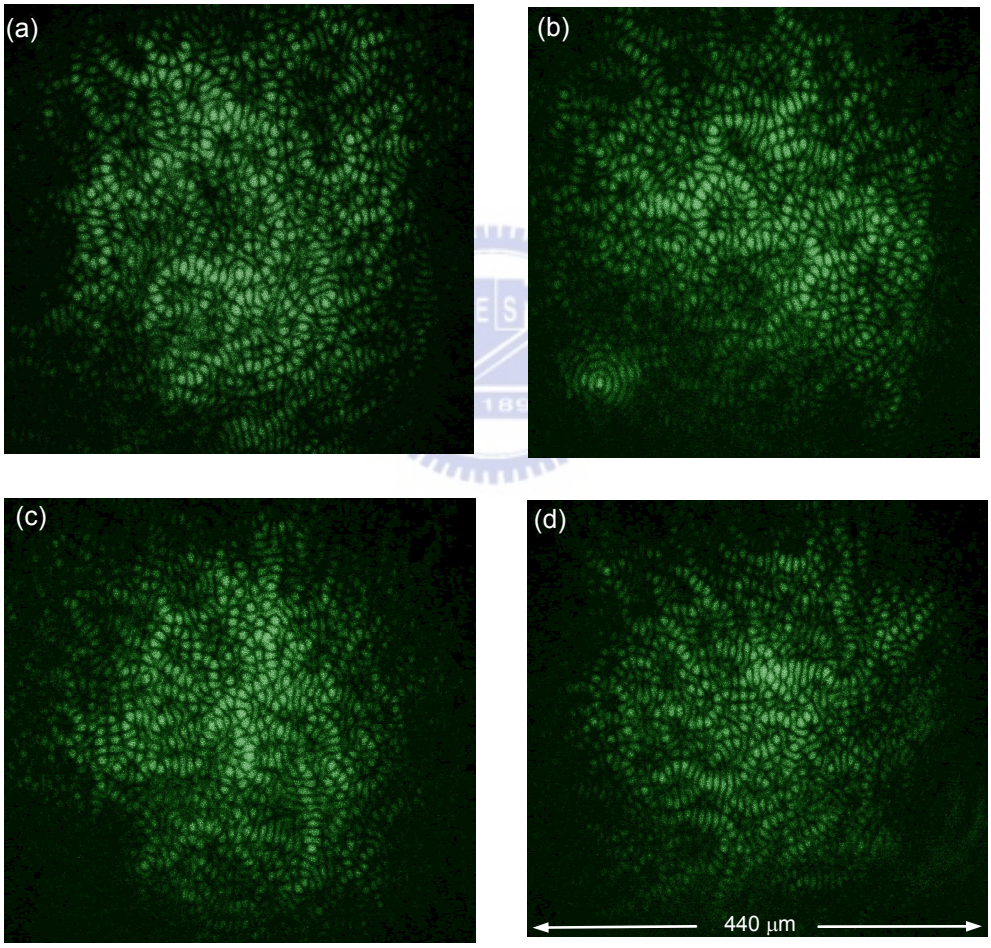

Fig. 5.3. Four examples of the near-field wave patterns measured at different transverse positions of the GdCOB crystal. (intensified image)

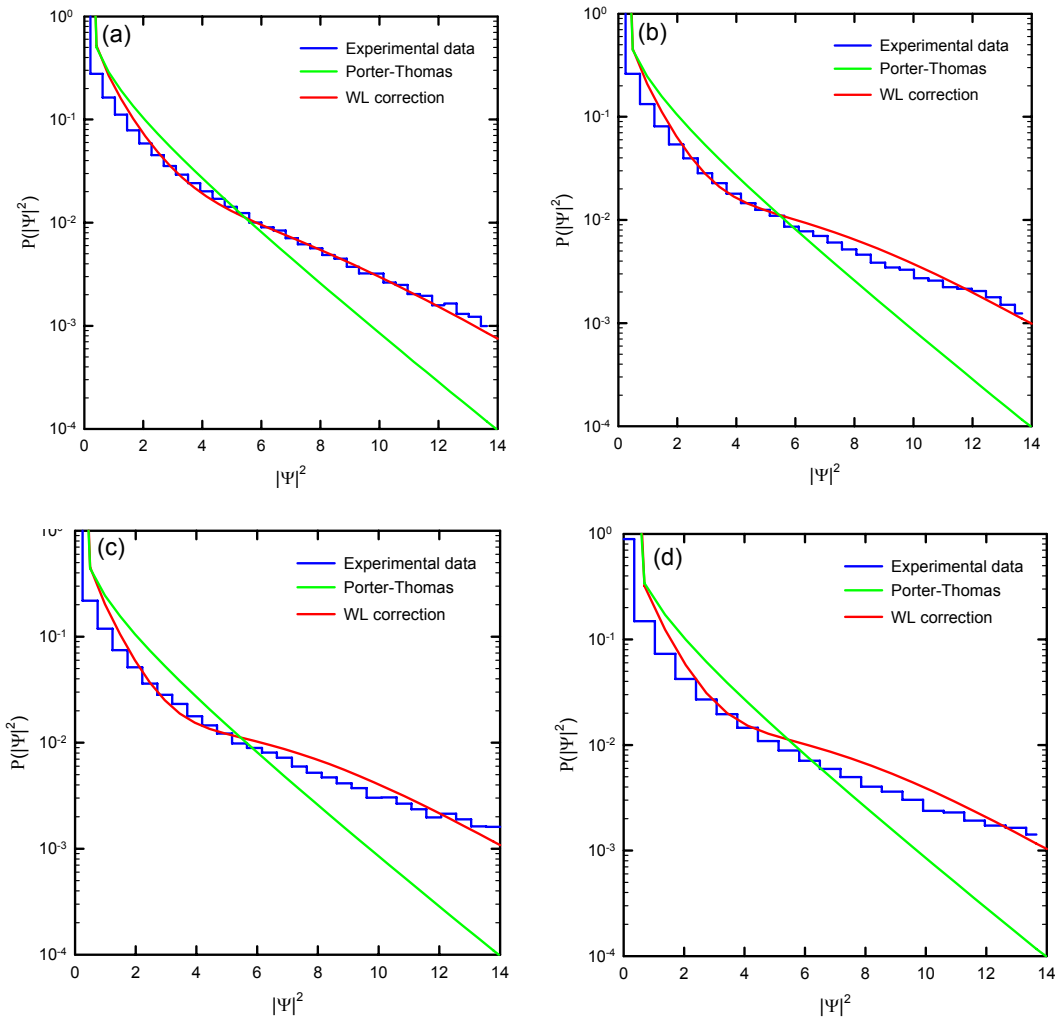

Fig. 5.4. (a)-(d) The density probabilities $P(I)$ for the experimental data shown in Figs. 3(a)-(d), respectively.

The density probability distribution $P(I)$ is extensively used to characterize the localization of the wave function, where $I = |\Psi|^2$. Fyodorov and Mirlin [15] found that the density probability distribution for the normalized disordered wave functions with WL can be expressed as

$$P_{FM}(I) = P_{PT}(I)\left[1 + (\mathrm{IPR} - 3)\left(\frac{1}{8} - \frac{1}{4}I + \frac{1}{24}I^2\right)\right], \quad (1)$$

where $P_{PT}(I) = \exp(-I/2)/\sqrt{2\pi I}$ is the classic Porter-Thomas (PT) distribution and $\mathrm{IPR} = \int I^2 d^2 r$ is the inverse participation ratio that is closely linked to the degree of localization. The IPR for chaotic systems can be immediately obtained from PT distribution, i.e. $\mathrm{IPR} = \int_0^\infty I^2 P_{PT}(I)\, dI = 3.0$, which is a universal value. The IPR is inversely proportional to the volume in which the wave function is confined. As a consequence, the IPR values for disordered systems are generally greater than 3.0 and large IPR values correspond to strongly localized states. We analyzed the experimental near-field patterns to obtain the density probability distribution. Figures 5.4 (a)-(d) display the density probabilities $P(I)$ for the experimental data shown in Figs. 3(a)-(d), respectively. The IPR values for the experimental wave patterns in Figs. 5.3 (a)-(d) are 4.39, 4.91, 5.35, and 5.67, respectively. All four intensity distributions clearly deviate from the PT distribution but show fairly good agreement with the theoretical distribution $P_{FM}(I)$. The good agreement indicates that the localization effect plays an important role for conical SHG in disordered domain structures.

With the experimental near-field patterns, we calculated the intensity correlation function (ICF) to get further information about the disordered wave function. The ICF for the normalized wave function is defined as $C(\Delta r) = \langle I(\vec{r}) I(\vec{r}\,') \rangle - 1$, where $\Delta r = |\vec{r} - \vec{r}\,'|$. The ICF $C(\Delta r)$ for disorder systems is composed of three terms describing short-range $C_1(\Delta r)$, long-rang $C_2(\Delta r)$, and infinite-range $C_3(\Delta r)$ [19]. For the 2D orthogonal case, $C_1(\Delta r)$ is given by $2J_0(K\Delta r)$, where J_0 is the Bessel function of zero order. Note that the ICF for chaotic systems is only contributed by $C_1(\Delta r)$. Figure 5.5 shows the measurement of $C(\Delta r)$ for the experimental wave patterns shown in Figs. 3 (a)-(d). Since $C(\Delta r)$ at $\Delta r = 0$ is equal to the value of $(\mathrm{IPR} - 1)$, the increase of the short-range correlation due to localization is perceptible. A more intriguing feature is that the measured $C(\Delta r)$ are found to approach a constant value for long range. The spatial dependence of the long-range contribution can be examined from the difference $C(\Delta r) - C_1(\Delta r)$, as shown in Figure 5.6. It can be seen that the long-rang contribution depends on the

degree of localization and its magnitude increases with increasing the IPR value. The similar long-range correlation has also been observed in the transmission of microwaves [20]. Although numerical study of light in a random medium reveals the analogous phenomenon [21], the present investigation provides the first experimental evidence for the long-range correlation due to transverse localization.

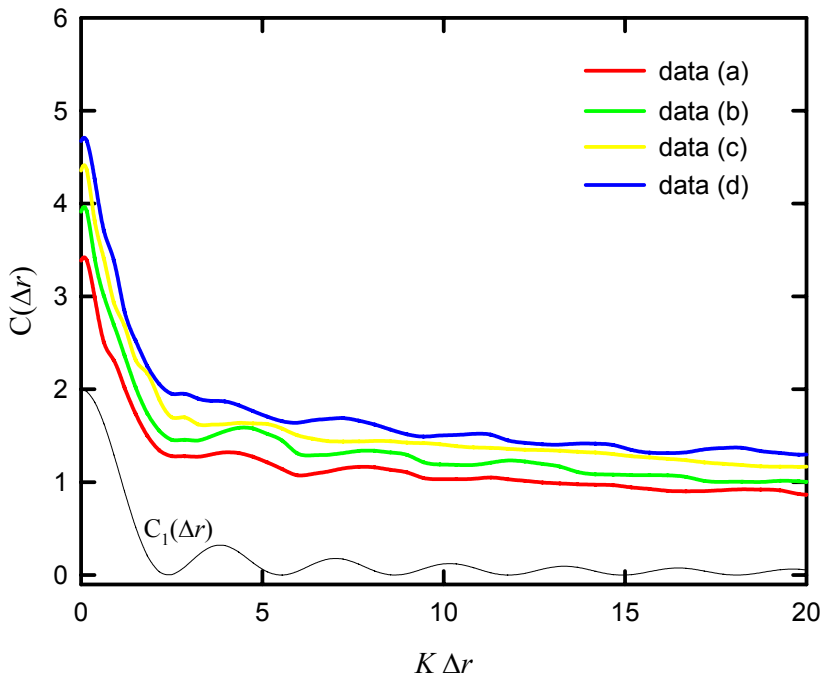

Fig. 5.5. The measurement of intensity correlation function $C(\Delta r)$ for the experimental wave patterns shown in Figs. 3 (a)-(d).

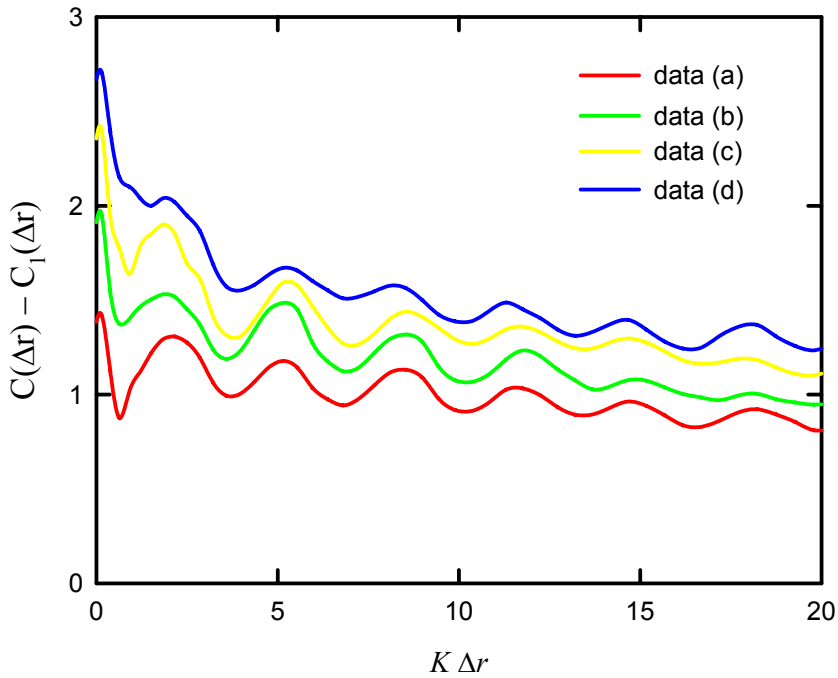

Fig. 5.6. The difference $C(\Delta r) - C_1(\Delta r)$.

5.2.4 Conclusion

In summary, the spatial structure of 2D disorder wave functions with weak localization has been explored with the conical SHG of laser in random domain structures. The statistics of the experimental near-field patterns are found to be in quantitative agreement with the theoretical distributions with the correction of weak localization. Furthermore, the analysis of the ICF reveals that the localization effect not only increases the magnitude of the short-rang correlation but also introduces a nearly constant value to the long-range correlation. The present result also confirms the possibility of using conical SHG as a diagnostic tool for topographical characterization of crystals in which localization phenomenon occurs naturally.

5.2.5 Classification of Corresponding Far-field and Near-field Pattern of Conical SHG in GdCOB and BBO crystal (Future Work)

We found new patterns differ from pattern described by order parameter equations (OPEs) or complex Ginzburg-Landau equations in other physical system such as [44,46]. Several pictures showed in Fig. 5.7.

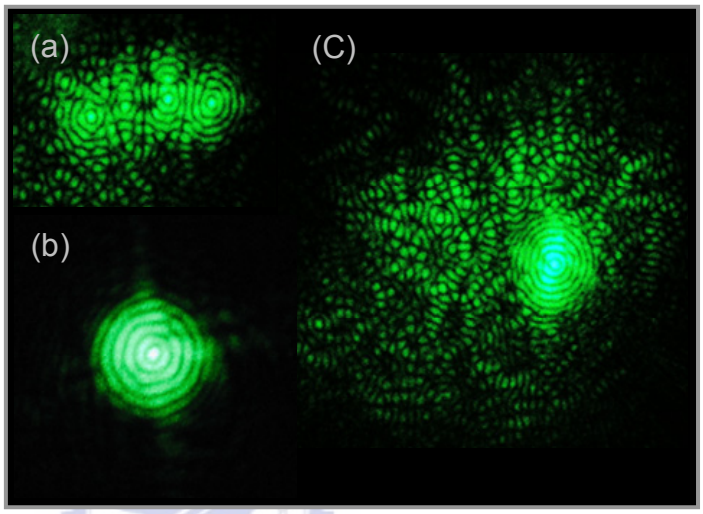

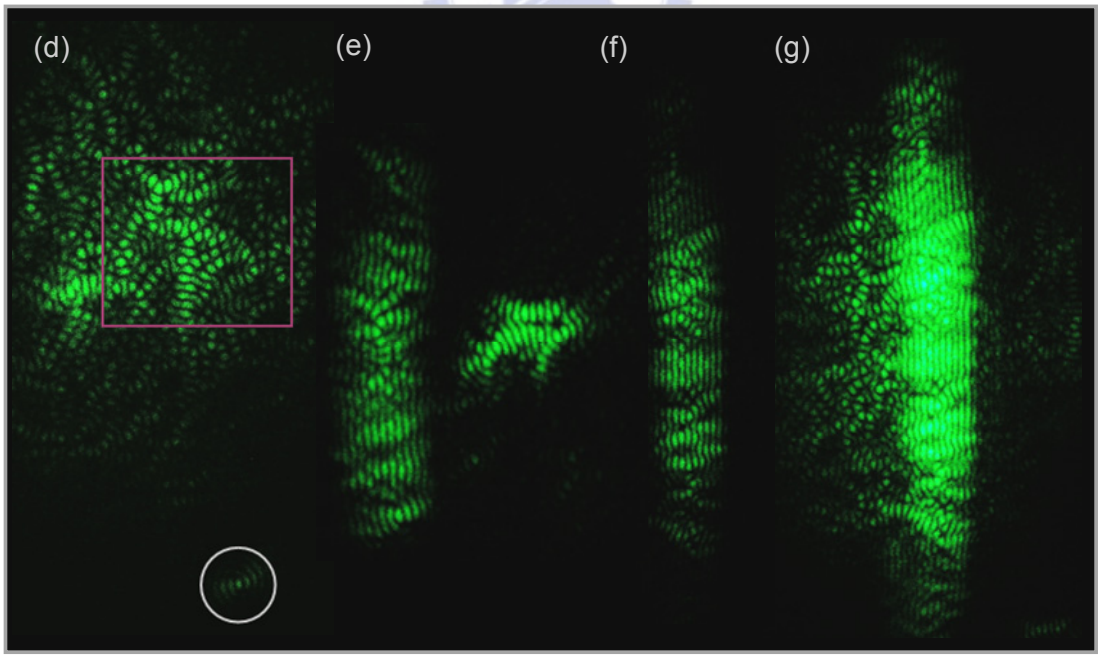

Fig. 5.7. Several pictures of other typical strong localization and weak localization patterns for classifications.

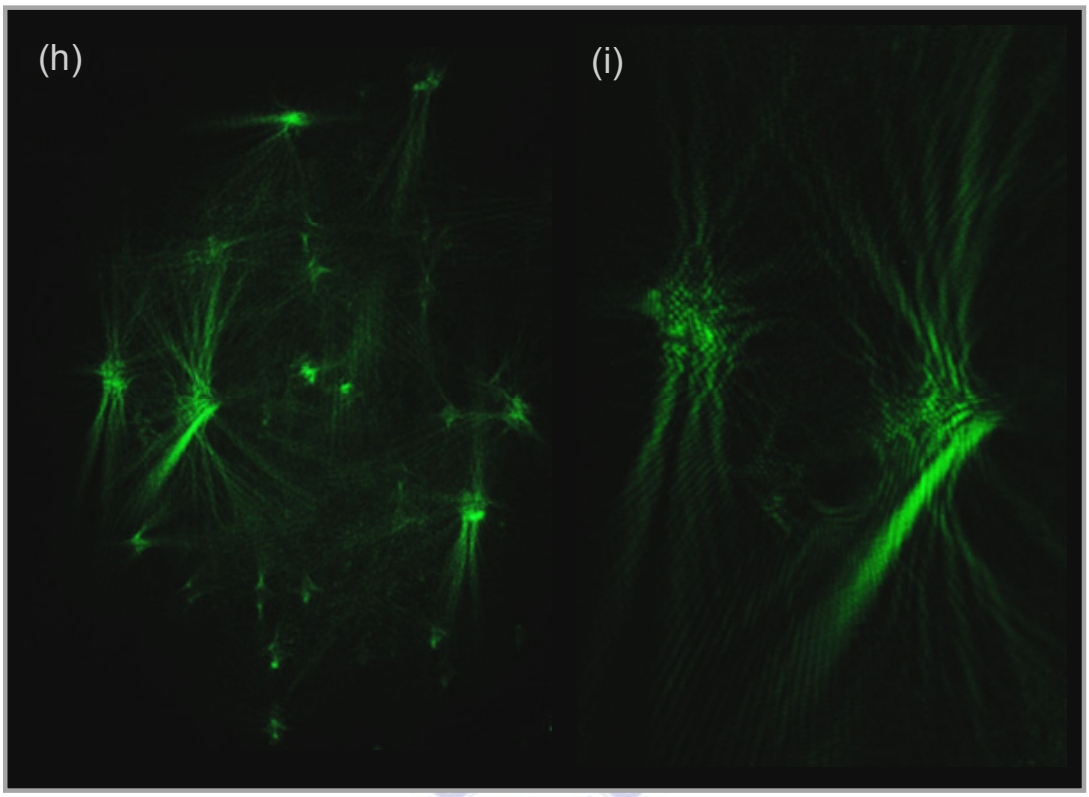

Fig. 5.7. Several pictures of other typical strong localization and weak localization patterns for classifications.

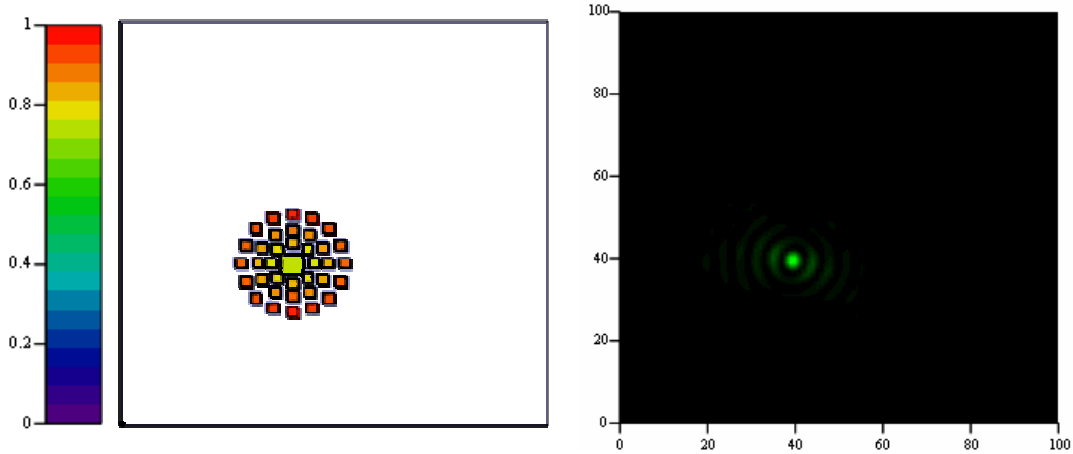

Fig. 5.8. Reveal near-field pattern in crystal by use of expansion method with given potential.

5.2.6 Reveal Near-field Pattern in Crystal by use of Expansion Method with Random Scattering (Future Work)

We try to use expansion method [50-52] with given potential to reveal near-field pattern in crystal from random scattered conical SHG. (also in unsymmetrical double-cladding or passive fiber). Several test results of strong localized near-field pattern were showed in Fig. 5.8-5.9. Another reconstruction of near-field and corresponding far-field patterns was demonstrated in Ref. [52] for quantum billiard.

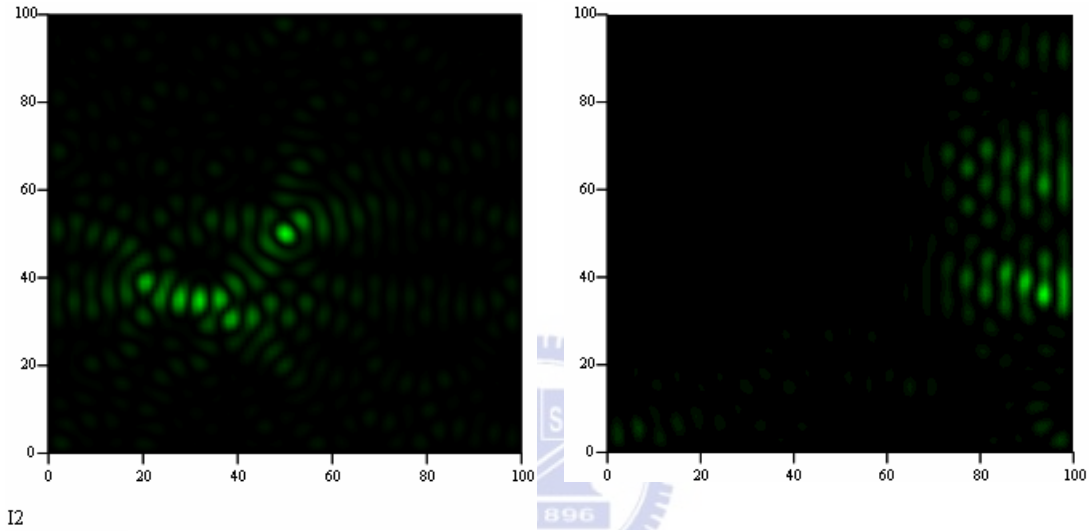

Fig. 5.9. Reveal near-field pattern in crystal by use of expansion method with given potential.

5.2.7 Information of Crystal Property from Noncoaxial Conical SHG and Phase Matching (Future Work)

We try to study the information of crystal optical property or birefringence from non-coaxial conical SHG and PM. Some theories about non-coaxial conical PM had been published a decade ago [47]. The offset angle and divergent angle of conical SHG from different experimental results seems had consistence.

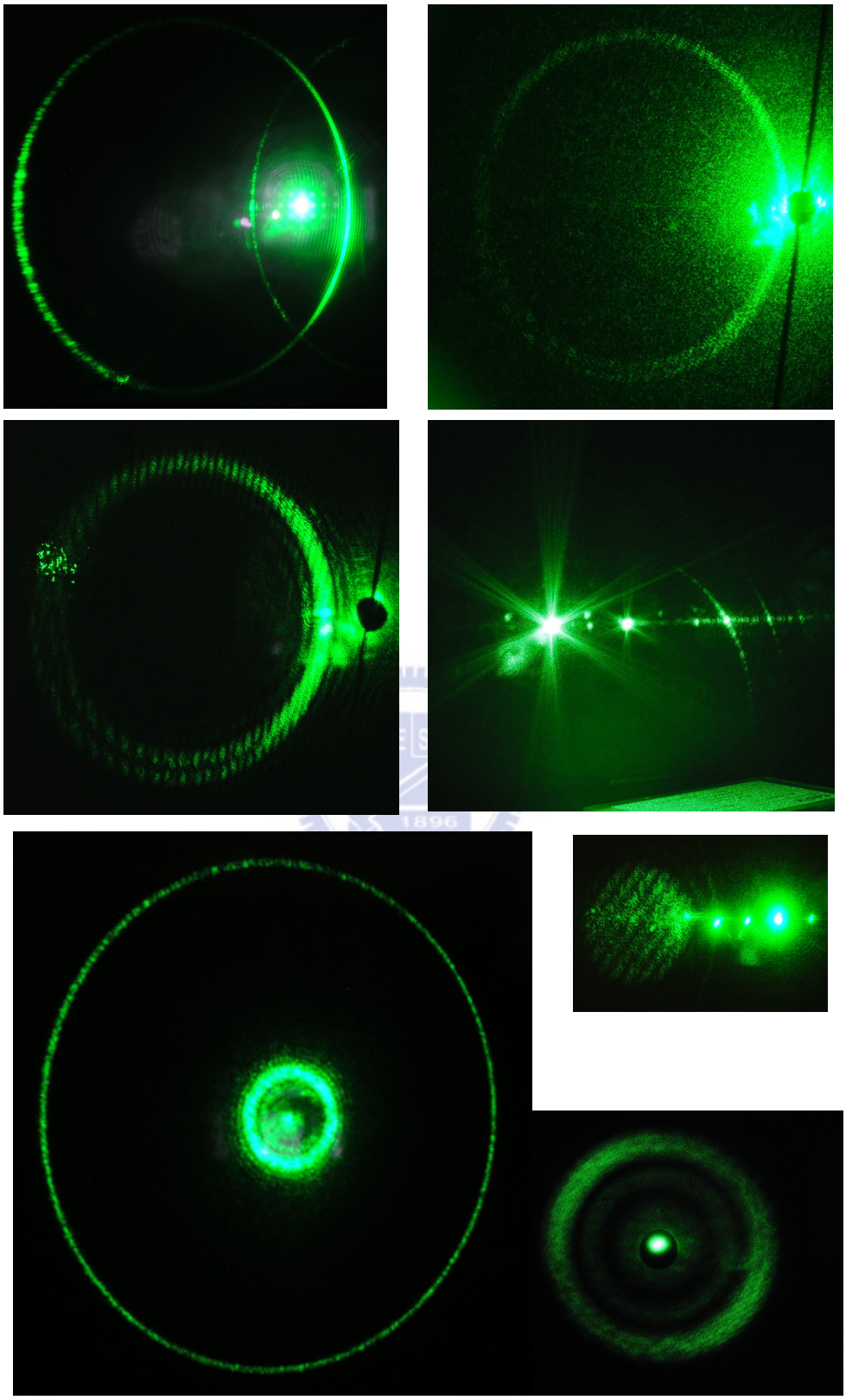

Fig. 5.10. Experimental far-field patterns in a crystal such as Gd:COB, BBO, SBN...etc., which include non-coaxial/coaxial conical SHG.

5.3 Optical Parametric Oscillator

Two beams termed "pump" and "signal" wave with different frequencies (ν_p, ν_s) incident on a nonlinear crystal will generate a traveling polarization wave termed "idler" at the difference frequency (ν_i). The idler wave can mix with the pump beam to produce a traveling polarization wave at the signal frequency. The process continues growing up signal and idler waves and wearing pump wave in the crystal as a function of distance. Each of three generated polarization waves travel at the same velocity is required for considerable parametric amplification. So that the k vectors satisfy the momentum conservation condition $k_p = k_s + k_i$. Because the pump wave with photon energy $h\nu_p$ is generating signal and idler waves, energy conservation requires $\nu_p = \nu_s + \nu_i$. Put the parametric amplification in a resonant cavity designed for a certain frequency will form the optical parametric oscillator (OPO). The OPO laser transform a pump photon into a signal and a idler photon, and amplify the signal photons. The idler and signal frequency is tunable through phase-matching condition. Due to three photon process without radiation transition, quantum efficiency can close to 100%. [48,B1]

5.4 150-kW Compact Efficient Eye-safe Laser with a shared cavity configuration Pumped by Laser Diode-stack

Compact nanosecond pulsed lasers operating with emission at the eye-safe wavelength region (1.5-1.6 μm) are of great interest for many applications such as laser radar, active imaging, and remote sensing [23,24]. The methods for generating eye-safe lasers include the solid-state lasers with Er^{3+}-doped or Cr^{4+}-doped media [25-28] and the Raman lasers pumped by Nd-doped lasers [29-32]. Another promising approach for high-peak-power eye-safe laser sources is based on intracavity OPO [33-38]. The advent of high damage threshold nonlinear crystals and diode-pumped Nd-doped lasers leads to a renaissance of interest in intracavity OPO's. Recently, we demonstrated a compact efficient eye-safe OPO pumped by a diode-pumped passively Q-switched Nd:GVO_4 laser to produce peak powers at 1573 nm higher than 10 kW [39]. However, the applications for long-distance laser rangefinders require pulse energies in the mJ range and peak powers greater than 100 kW [24].

The conventional configurations for intracavity OPO pumped by Q-switched Nd-doped lasers [33-39] are based on the coupled cavity configuration in which there are separate resonators for the signal and fundamental optical fields. However, the amplitude stability of the signal outputs for the coupled cavity configuration is

severely dependent on the cavity alignment because the resonator lengths and the longitudinal-mode spacing are different for the pump and signal beams. Recently, it was confirmed [40] that the shared cavity configuration in which the pump and signal beams share the same resonator provides a substantially superior amplitude stability, in comparison with the coupled cavity configuration. Therefore, it is of practical interest to develop the eye-safe intracavity OPO in the mJ range with the shared cavity configuration.

In this work we use a shared resonator configuration to construct a compact intracavity OPO in the mJ range. A lens duct is designed to be an efficient coupling lens for the diode-pumped passively Q-switched Nd:YAG/Cr^{4+}:YAG laser. With the passively Q-switched laser to pump the intracavity OPO, 3.3 mJ pulses with 150 kW peak power at 1573 nm is generated. The effective conversion efficiency with respective to the optimized pulse energy form the passively Q-switched 1064 nm laser is up to 51%.

5.4.1 Experimental setup of intracavity OPO

The pump source is a quasi-cw high-power diode stack (Coherent G-stack package) that consists of six 10-mm-long diode bars generating 80 W per bar, for a total of 480 W at the central wavelength of 808 nm. The diode stack is designed with 0.4 mm spacing between the diode bars so the overall area of emission is approximately 10 mm (slow axis) × 2.4 mm (fast axis). The full divergence angles in the fast and slow axes are approximately 35° and 10°, respectively. A lens duct was designed to efficiently couple the pump radiation from the diode stack into the laser crystal. As shown in Fig. 5.11, there are five geometric parameters, r, L, H_1, H_2, and H_3, for a lens duct, where r is the radius of the input surface, L is the length of the duct, H_1 is the width of the input surface, H_2 is the width of the output surface, and H_3 is the thickness of the duct [41,42]. With the ray-tracing analysis [42], the coupling efficiency was found to be up to 87% for a lens duct with the parameters of r = 10 mm, L = 32 mm, H_1 = 12 mm, H_2 = 2.7 mm, and H_3 = 3 mm. Based on the theoretical result, a lens duct was manufactured and used in the experiment.

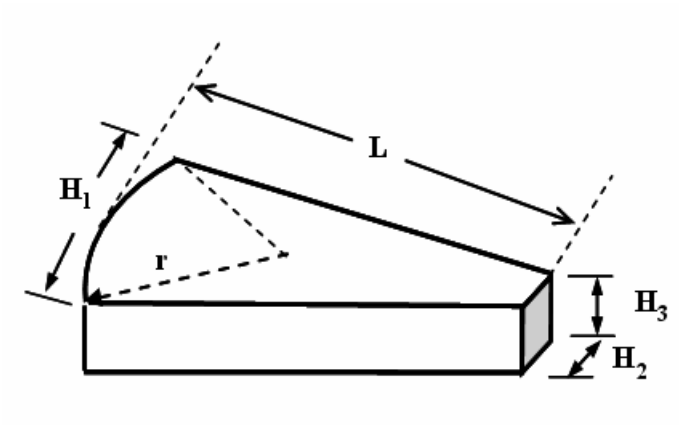

Fig. 5.11. Schematic of a lens duct in which r is the radius of the input surface, L is the length of the duct, H_1 is the width of the input surface, H_2 is the width of the output surface, and H_3 is the thickness of the duct.

Figure 5.12 (a) shows the experimental setup of the intracavity OPO pumped by a diode-pumped passively Q-switched Nd:YAG/Cr^{4+}:YAG laser in a shared cavity configuration. The fundamental laser cavity was formed by a coated Nd:YAG crystal and an output coupler. The OPO cavity entirely overlapped with the fundamental laser cavity. The Nd:YAG crystal had a 1.0 at. % Nd^{3+} doping concentration, a diameter of 5 mm, and a length of 10 mm. To setup the shared cavity, the incident side of the laser crystal was coated to be highly reflective at 1064 nm and 1573 nm (R>99.8%) and highly transmitted at the pump wavelength of 808 nm (T>90%). The other side of the laser crystal was coated to be antireflective at 1064 nm and 1573 nm (R<0.2%). A KTP crystal was used to be the nonlinear crystal of the OPO. The KTP crystal, 4×4×20 mm^3, was employed in type II noncritical phase-matching configuration along the x-axis ($\theta = 90^\circ$ and $\phi = 0^\circ$) to have both a maximum effective nonlinear coefficient and no walk-off between the pump, signal, and idler beams. On the other hand, a Cr^{4+}:YAG crystal was used to serve as a saturable absorber for passive Q-switching. The Cr^{4+}:YAG crystal had a thickness of 3 mm with 60% initial transmission at 1064 nm. Both sides of the KTP and Cr^{4+}:YAG crystals were coated for antireflection at 1573 nm and 1064 nm. The output coupler had a dichroic coating that was highly reflective at 1064 nm (R>99.8%) and partially reflective at 1573 nm (R=60%). All crystals were wrapped with indium foil and mounted in conductively cooled copper blocks. The total cavity length was approximately 50 mm.

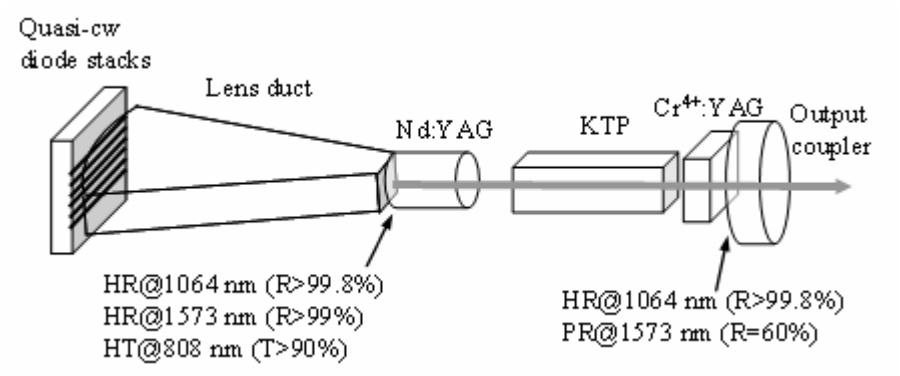

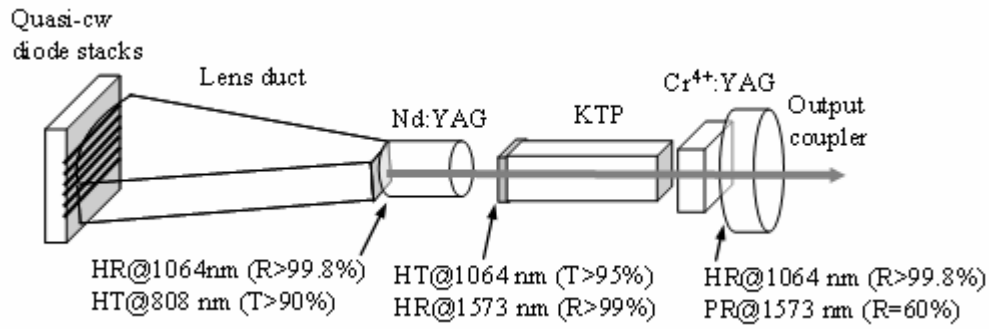

Fig. 5.12. Schematic of the intracavity OPO pumped by a diode-pumped passively Q-switched Nd:YAG/Cr^{4+}:YAG laser, (a) the shared cavity, (b) the coupled cavity.

For comparison, the conventional coupled cavity configuration is depicted in Fig. 5.12 (b). It can be seen that the OPO cavity in the coupled resonator configuration was formed by a coated KTP crystal and an output couplerl and the OPO cavity length was about 25 mm. One side of the KTP crystal was coated to have high reflection at the signal wavelength of 1573 nm (R>99.8%) and high transmission at the pump wavelength of 10643 nm (T>95%). The other side of the KTP crystal was coated for antireflection at 1573 nm and 1063 nm.

The pulse temporal behavior at 1063 nm and 1571 nm was recorded by a LeCroy digital oscilloscope (Wavepro 7100; 10 G samples/sec; 1 GHz bandwidth) with a fast InGaAs photodiode. The spectral information of the laser was monitored by an optical spectrum analyzer (Advantest Q8381A). The spectrum analyzer employing diffraction grating monochromator can be used for high-speed measurement of pulse light with the resolution of 0.1 nm.

5.4.2 Experimental results

First of all, the quasi-cw free-running operation without KTP and Cr^{4+}:YAG crystals was performed to confirm the pumping efficiency of the lens duct and the quality of the laser crystal. For this investigation the diode stack was derived to emit optical pulses 200 μs long, at a repetition rate of 100 Hz, with a maximum duty cycle of 2%. Furthermore, an output coupler with 96% reflectivity at 1064 nm was used instead of the above-mentioned OPO output coupler. Figure 5.13 plots the experimental results of the free-running operation for the output average power as a function of the diode pump power. It can be seen that the output power of 160 W was achieved at an incident pump power of 360 W. The overall slope efficiency was found to be as high as 45%. The fairly good efficiency affirms the pump scheme to be practical.

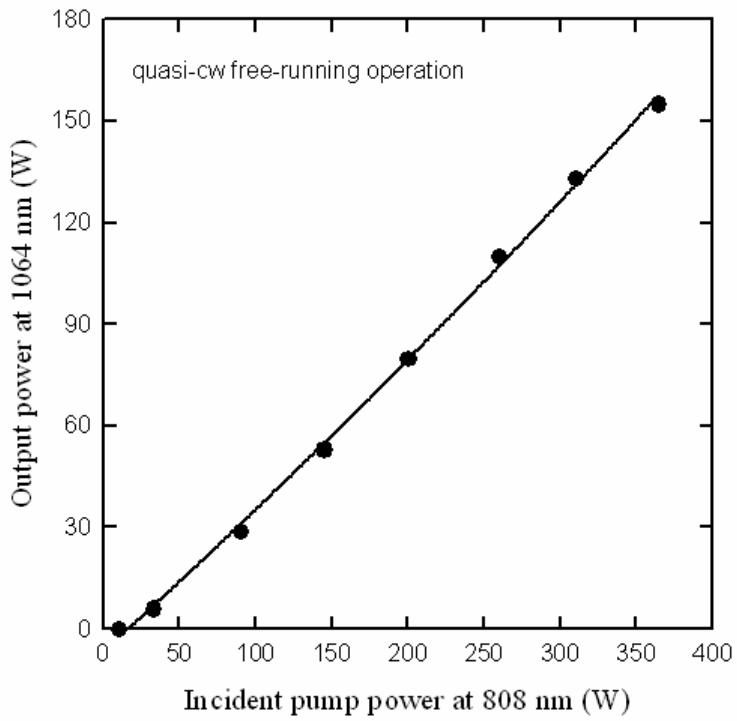

Fig. 5.13. Output power at 1064 nm with respect to the incident pump power at 808 nm for quasi-cw free-running operation.

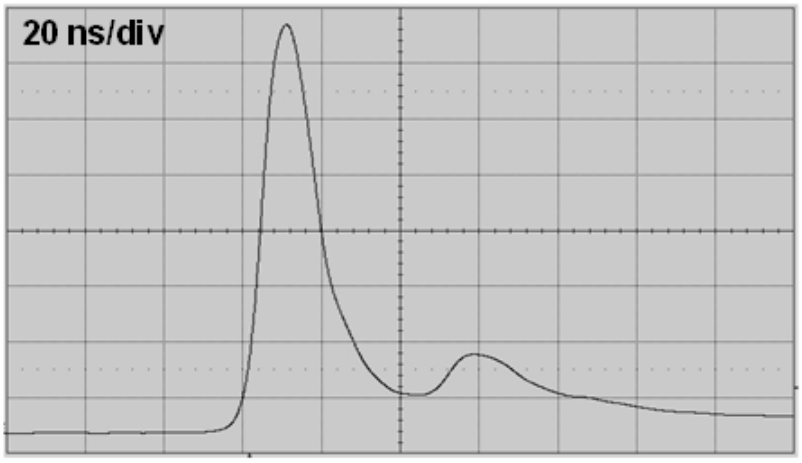

Fig. 5.14 Temporal shape for the passively Q-switched Nd:YAG/Cr^{4+}:YAG laser at 1064 nm.

We estimated the performance of the passively Q-switched Nd:YAG/Cr^{4+}:YAG laser before the intracavity OPO experiment. For this investigation an output coupler with partial reflection at 1064 nm was used and the diode stack was derived to emit optical pulses 250 μs long, at a repetition rate of 10 Hz. The optimum Q-switched performance at 1064 nm provides the baseline for evaluating the conversion efficiency of the intracavity OPO. The optimum reflectivity of the output coupler was found to be approximately 60%. The threshold of the Q-switched laser operation was found to be approximately 102 mJ and the output pulse energy at 1064 nm was measured to be 6.5 mJ. As shown in Fig. 5.14, the effective pulse width was found to be approximately 19 ns; consequently, the peak power was up to 330 kW.

With an OPO output coupler, the intracavity OPO experiment was performed. The threshold of the intracavity OPO was found to be nearly the same as that of the passively Q-switched laser. The output pulse energy of the signal wave at 1573 nm was measured to be 3.3 mJ. The effective conversion efficiency with respect to the optimized pulse energy from the passively Q-switched laser is up to 51%. For the coupled cavity [34], the conversion efficiency was found to be approximately 26%. In other words, the conversion efficiency of the shared cavity configuration is significantly superior to that of the coupled cavity configuration. The typical result for the optical spectrum measurement is depicted in Fig. 5.15. Figure 5.16 shows the temporal shapes of the laser and signal pulses. It can be seen that the signal output consisted of a short intensive leading peak accompanied with a long weak ripple.

With the numerical integration, the signal peak power was calculated and found to be approximately 150 kW. The signal peak power is expected to be enhanced by use of an output coupler with a lower reflectivity at the signal wavelength. The spatial distribution of the signal output was recorded with an infrared CCD and displayed in Fig. 5.17. The beam quality M^2 factor was estimated to be approximately 1.5.

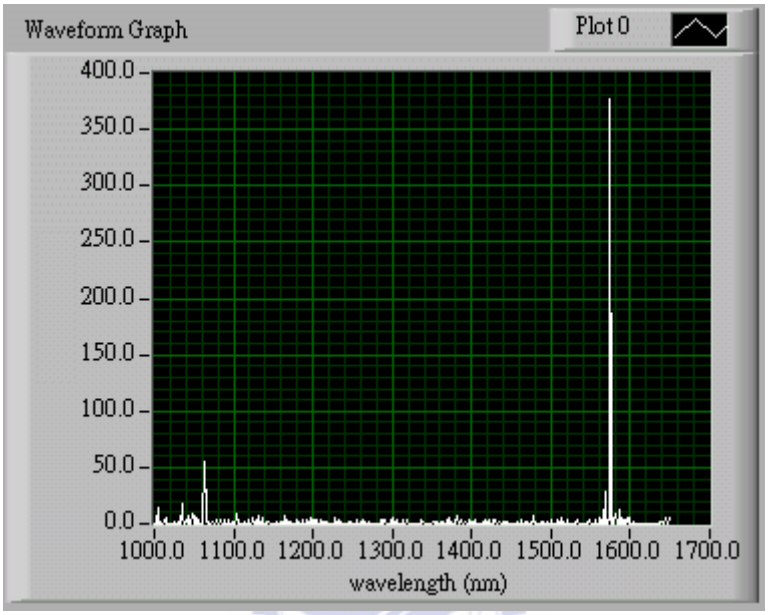

Fig. 5.15. Optical spectrum measurement for the intracavity OPO.

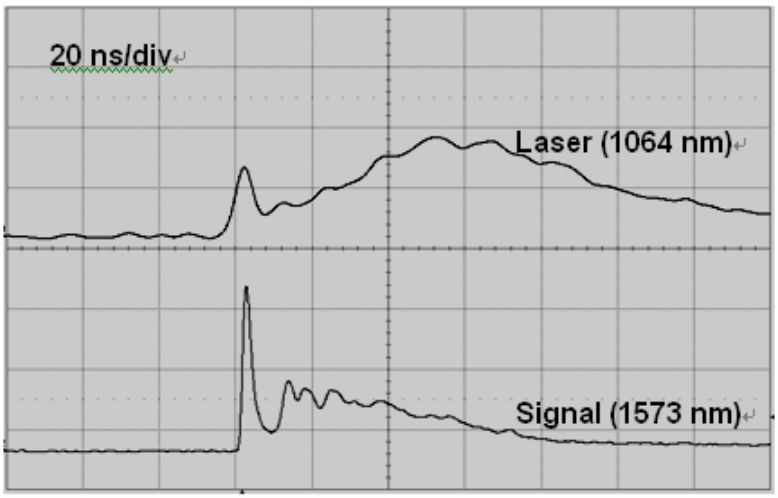

Fig. 5.16. Typical temporal shapes for the laser and signal pulses.

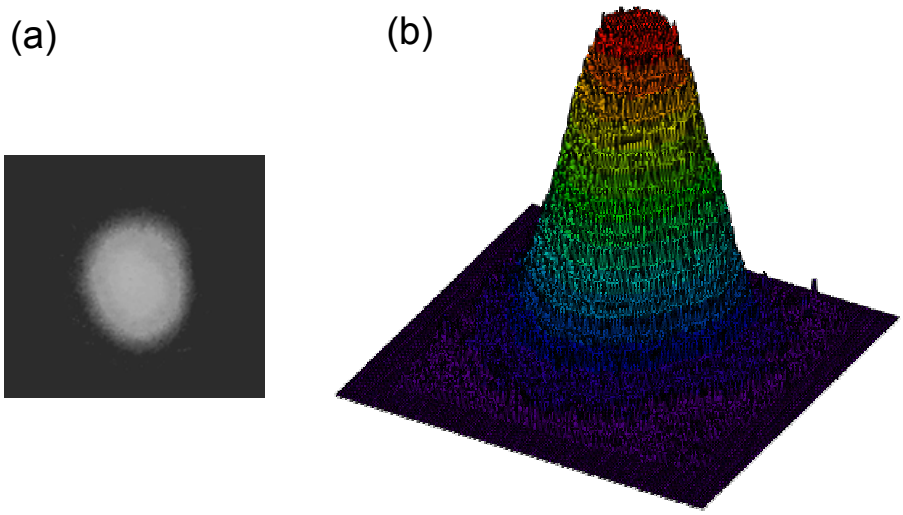

Fig. 5.17. Experimental far-field pattern of the signal output pulse (a) 2D image, (b) 3D representation.

5.4.3 Conclusions and Future Work

We have employed a diode-pumped passively Q-switched Nd:YAG laser to pump an intracavity OPO in a shared cavity configuration. A lens duct has been designed to efficiently couple the pump radiation from the diode stack into the laser crystal. A slope efficiency of 45% has been obtained for the quasi-cw free-running operation in the fundamental mode lasing. For the Q-switching operation at 1064 nm, the cavity produced 6.5 mJ pulses with 330 kW peak power. With the Q-switched laser to pump the OPO at 1573 nm, 3.3 mJ pulses with 150 kW peak power have been achieved, corresponding to an effective conversion efficiency of 51% with respect the optimized pulse energy at 1064 nm.

In the future, two targets we want to dead on. The first one is promoted pulse energy of >10 mJ for modern air-defense Ladar. According to modeled results of range performance for micro laser range finder (μLRF) system with a 1‰ false alarm rate [49], using a 1 inch receiver PIN InGaAs detector system and the minimum required range specified as 1.5 km, the model indicates about 0.5 mJ laser output will be sufficient to perform as required. Under conditions of clear (23 km) / impaired (7 km) visibility, to reach a goal of 3.5 km, about 2 mJ / 4 mJ are required. While a 1

inch receiver APD InGaAs detector system is used, only 0.4 mJ / 0.9 mJ is needed to reach 3.5 km. High pulse energy is important to long rage detection. The second one is using the semiconductor QWs as a passive Q-switch for eye-safe Nd:YVO_4 (and deservedly Nd:YAG) OPO. Up to now, we have accomplish >mJ-level Nd:YVO_4 Q-switched laser with a pulse width < 2 ns at 1064 nm by use of a SESA. However, to make process of OPO happened or to reduce the threshold of OPO might need support of the design of SESA.